

# A Region of Interest Strategy for Minimizing Resolution Distortions in Quantitative Myocardial PET Studies

Gary D. Hutchins, John M. Caraher, and Raymond R. Raylman

*University of Michigan Medical Center, Department of Internal Medicine, Division of Nuclear Medicine, Ann Arbor, Michigan*

The distortions inherent in PET images of the human heart due to finite image resolution and cardiac motion limit the capability to evaluate physiology quantitatively. A method based on a simple geometrical model of region of interest representations in physical space has been developed to minimize these distortions. In this paper, simulation studies have been performed to evaluate the noise characteristics of the method. This study demonstrates that unbiased estimates of kinetic model parameters which describe myocardial physiology can be measured with an accuracy of 7%–15% for scale-related parameters and 4%–16% for shape-related parameters of kinetic models in studies with the equivalent of 1 million events. Application of the techniques developed in this paper for the measurement of myocardial blood flow in eight dogs (14 independent flow states) shows a strong correlation with microsphere determined blood flow in the same animals (slope = 1.022, intercept = -0.18,  $r = 0.96$ ).

**J Nucl Med 1992; 33:1243–1250**

**D**istortion of myocardial PET images by finite image resolution (PET scanner, cardiac, and respiratory motion) represents a serious limitation to quantitative studies of physiology and biochemistry (1–4). The resolution distortions are typically classified as the partial volume effect and tissue:blood spillover (5–15). Manifestations of these effects in dynamic studies of the heart are seen in the two principal properties of the myocardial tissue time-activity curves. These basic properties are the shape of the curve and its scale. The partial volume effect results in an underestimation of the radionuclide quantity in objects which are less than approximately two times the reconstructed image resolution (3). In myocardial PET studies, the wall of the left ventricle ranges from 0.8 cm to 1.2 cm in thickness, resulting in significant loss of quantitative information (5). Typical radionuclide concentrations extracted from PET images are only 50%–70% of the true

radionuclide concentrations (1). Therefore, the partial volume effect will be manifest primarily as a scale distortion on myocardial tissue time-activity curves. In contrast, the cross contamination of measured signal between myocardial tissue and right or left ventricle blood-pool produces tissue time-activity curves which are dramatically altered in shape. These shape distortions are the result of mixing two curves with very distinct kinetic properties (sharp bolus blood curve and a slow temporally varying tissue curve).

The difference between the two basic manifestations of resolution distortions in PET studies can be seen in the kinetic model parameter estimates from dynamic data. The scale-related distortions (partial volume effect) predominantly bias the uptake rate constant ( $K_1$ ) of kinetic models. The shape-related distortions produce biases in the kinetic rate constants which primarily describe the retention and washout of the tracer from the tissue ( $k_2 \dots k_n$ ).

At the present time, the most serious efforts to correct for the resolution distortion effects in kinetic PET studies have been associated with methods for the measurement of myocardial blood flow (11–15). In the mathematical formulation of the equations used in each of these methods, the measured PET signal is assumed to be a linear combination of the myocardial and blood-pool tracer concentrations. In the implementation of these methods, the fractional contribution of the blood-pool to the PET signal is either measured using equilibrium blood-pool studies (11,15), calculated based upon the geometry of the heart and tomograph resolution (13), or estimated as an additional parameter in the model (12). In several of these techniques, the myocardial tissue contribution to the PET signal is also estimated as another parameter in the model (11,12,15).

In an alternative method recently developed by Hutchins et al. (14), the blood-pool and myocardial tissue contribution to the measured PET signal are coupled through the use of a single additional parameter in the mathematical model fit to the measured data. In this paper, the method developed by Hutchins et al. (14) is examined in detail. This method reduces the bias introduced into ki-

Received Sept. 12, 1991; revision accepted Jan. 31, 1992.  
For reprints contact: Gary D. Hutchins, PhD, University of Michigan Medical Center, 3480 Kresge III, Box 0552, Ann Arbor, MI 48109-0552.

netic model rate constants by resolution distortions using a simple geometric model of the volume representation of a region of interest (ROI). The geometric model of the ROI volume is reduced in complexity through the use of assumptions regarding the tissue types which contribute signal to this volume. Optimization of the ROI position on heart images to meet the ROI model assumption has been evaluated using PET simulation methods. Simulation studies have also been performed to evaluate the influence of myocardial wall thickness and image resolution on this technique. Experimental verification of this ROI data analysis strategy is presented using  $^{13}\text{NH}_3$  and radiolabeled microsphere blood flow data measured in dogs.

## MATERIALS AND METHODS

### Geometric ROI Model

A simple model of the representation of an ROI in physical space is the basis of the method which has been developed to eliminate resolution distortions in myocardial PET studies (Fig. 1). The radionuclide concentration which is observed from the placement of an ROI over a heart image ( $C_{\text{PET}}(t)$ ) represents the weighted sum of the radionuclide concentrations for each tissue type which occupies the volume.

$$C_{\text{PET}}(t) = \sum_{i=1}^N F_i C_i(t). \quad \text{Eq. 1}$$

The weights in Equation 1 ( $F_i$ ) represent the fractions of the ROI volume occupied by the  $i^{\text{th}}$  tissue type ( $C_i(t)$ ). Therefore, assuming that the entire volume is occupied by a linear combination of multiple tissue types,

$$\sum_{i=1}^N F_i = 1.0. \quad \text{Eq. 2}$$

The expression in Equation 1 can be algebraically manipulated to form an equation which relates  $C_{\text{PET}}(t)$  to the true myocardial tracer concentration ( $C_m(t)$ ) and the blood-pool concentration ( $C_a(t)$ ).

$$C_{\text{PET}}(t) = F_a C_a(t) + F_m C_m(t) + \sum_{i=3}^N F_i C_i(t). \quad \text{Eq. 3}$$

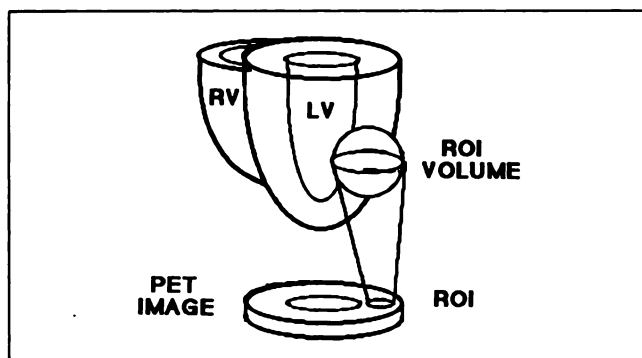


**FIGURE 1.** ROI representation in physical space. Placement of an ROI on a low-resolution cross sectional image has a true volume representation in space which is much larger than the originally defined ROI. The volume of this ROI is determined by the three-dimensional resolution of the imaging device.

If we assume that the terms in the summation on the right hand side of Equation 3 are negligible, then

$$C_{\text{PET}}(t) = F_a C_a(t) + F_m C_m(t). \quad \text{Eq. 4}$$

In this expression, the terms  $F_a$  and  $F_m$  represent the spillover of blood-pool activity into the ROI and the fraction of the volume which is occupied by myocardial tissue, respectively. Further simplification of this model can be achieved by strategically placing the ROI so that only myocardial tissue and blood pool occupy the ROI volume. Therefore, the fraction of the ROI volume that contains myocardium can be expressed in terms of the fraction of the ROI volume that is blood pool.

From Equation 2,

$$F_m = 1.0 - F_a - \sum_{i=3}^N F_i. \quad \text{Eq. 5}$$

$$\text{If } \sum_{i=3}^N F_i = 0,$$

$$\text{then } F_m = 1.0 - F_a. \quad \text{Eq. 6}$$

Substitution of Equation 6 into Equation 4 yields a new expression for the ROI tissue concentration ( $C_{\text{PET}}(t)$ ).

$$C_{\text{PET}}(t) = F_a C_a(t) + (1.0 - F_a) C_m(t). \quad \text{Eq. 7}$$

### PET Simulations

A series of simulation studies was performed to evaluate the error sensitivity of this myocardial data analysis strategy. The simulation studies consist of generating dynamic heart image data sets for predefined myocardial and blood kinetics, adding pseudorandom noise to the image data sets to generate multiple realizations, and fitting a kinetic model to the data to generate estimates of bias and variance in kinetic model parameter values. The process begins by assigning user selected kinetic properties to the blood pool and left ventricle of a segmented heart phantom model which mimics motion of the heart throughout the cardiac cycle. The tissue and blood kinetics are integrated over the time limits established by the scanning sequence and simulated radionuclide distributions are established. These distributions are input into a PET scanner simulation routine producing PET image sinograms (16).

### ROI Data Generation

To facilitate the rapid production of multiple data set realizations, an ROI method developed by Huesman was utilized (17). Predefined ROIs were forward projected and filtered to form an ROI sinogram. The ROI sinograms were then multiplied to the emission sinograms and the results integrated to produce mean values and standard deviations for each ROI position throughout the simulated dynamic imaging sequence.

Multiple kinetic time-activity curve realizations were generated by sampling Gaussian distributions with standard deviations determined using the Huesman algorithm. For each defined ROI, 500 noisy realizations were generated.

### Tissue and Blood Kinetics

Several combinations of tissue and blood kinetics were examined to evaluate the properties of the myocardial data analysis strategy. In all cases, the myocardial tissue kinetics were described by a simple two-compartment model. The values assigned for the rate constants are listed in Table 1. A continuously measured

**TABLE 1**  
Stimulation Study Rate Constants

| Configuration | $K_1$ (ml/g/min) | $k_2$ (min <sup>-1</sup> ) | BV   |
|---------------|------------------|----------------------------|------|
| A             | 1.0              | 1.0                        | 0.10 |
| B             | 1.0              | 0.33                       | 0.10 |
| C             | 1.0              | 0.20                       | 0.10 |
| D             | 1.0              | 0.14                       | 0.10 |
| E             | 1.0              | 0.11                       | 0.10 |
| F             | 0.2              | 0.022                      | 0.10 |
| G             | 0.6              | 0.066                      | 0.10 |
| H             | 3.0              | 0.33                       | 0.10 |
| I             | 5.0              | 0.55                       | 0.10 |

input function from an  $H_2^{15}O$  PET study performed in our laboratory (18) was used as the arterial blood curve in the simulations (Fig. 2). The simulated myocardial tissue time-activity curves studied are shown in Figure 3. Ten percent of the myocardial tissue was assumed to be occupied by vascular blood (BV).

### Parameter Estimation

Kinetic model parameters were estimated using a nonlinear curve fitting method based upon the Marquardt algorithm (19). Each ROI curve realization was fit with Equation 8:

$$C_{PET}(t) = (1 - F_a) \int_{t_1}^{t_2} K_1 e^{-k_2 t} \otimes C_a(t) dt + F_a \int_{t_1}^{t_2} C_a(t) dt. \quad \text{Eq. 8}$$

In each case, the parameters  $K_1$ ,  $k_2$ , and  $F_a$  were estimated. Mean and standard deviations for 500 realizations of each ROI curve were calculated to assess the bias and variance in model parameter estimates. The term  $F_a$  represents both the ventricle blood pool as well as the vascular fraction of the myocardial tissue (14).

### ROI Location

In each study, a series of ROIs was placed across the myocardium starting in the left ventricle blood-pool and projecting radially outward across the epicardial surface of the heart (Fig. 4). Each ROI was shaped like a sector of an annulus and had an area of 1.1 cm<sup>2</sup>. This strategy for the placement of ROIs enables the assessment of the performance of this method as a function of ROI position.

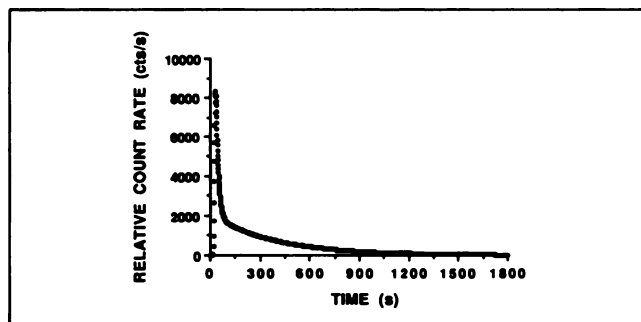


**FIGURE 2.** Arterial blood curve. This curve was derived from the continuous measurement of arterial blood following a bolus injection of  $H_2^{15}O$  into a human subject.

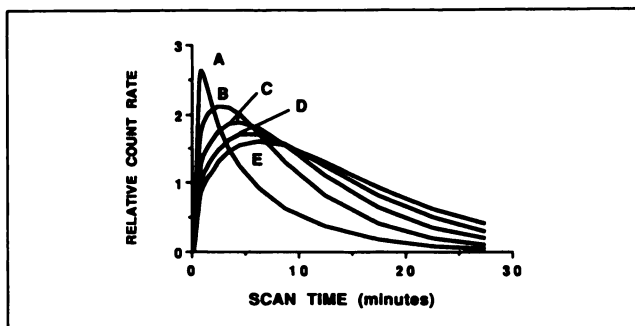


**FIGURE 3.** Simulated myocardial tissue time-activity curves. Each curve represents the convolution of a two-compartment mathematical model with the arterial blood curve. In each case, the  $K_1$  value is 1.0 ml/g/min. The  $k_2$  values for each curve are (A) 1.0 min<sup>-1</sup>, (B) 0.33 min<sup>-1</sup>, (C) 0.20 min<sup>-1</sup>, (D) 0.14 min<sup>-1</sup> and (E) 0.11 min<sup>-1</sup>.

### Wall Thickness Simulations

The effect of myocardial wall thickness on the ROI estimation strategy was evaluated by estimating the fraction of the ROI volume occupied by the blood pool at a point at which 95% of the ROI volume was occupied by myocardial tissue and blood.

$$F_a + F_m = 0.95. \quad \text{Eq. 9}$$

$$\sum_{i=3}^N F_i = 0.05. \quad \text{Eq. 10}$$

In this simulation, a step response function interface between myocardial tissue and blood pool was assumed. The tomograph resolution response function was Gaussian shaped with FWHM values ranging from 4 mm to 14 mm. Myocardial wall thicknesses ranging from 2 mm to 20 mm were simulated.

### Experimental PET Studies

Data from eight open-chest anesthetized dogs (14 individual flow states) were evaluated using the ROI strategy described in this paper. Each dog had ammonia and radiolabeled microsphere blood flow studies (20). The ammonia blood flow estimates were calculated using a three-compartment model (14) with the  $K_1$  estimates representing myocardial blood flow. A range of myocardial blood flows was created through pharmacologic stimula-

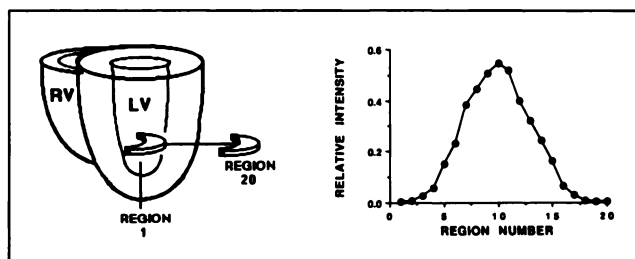


**FIGURE 4.** ROI definitions. The definition of the ROI positions used in the simulation studies starts in the left ventricle blood pool (region 1) and steps across the myocardium. Each ROI is shaped like a sector of an annulus and has an area 1.1 cm<sup>2</sup>. The solid circles on the plot represent the position of the center of the ROI drawn over an image profile of the myocardium. Region 10 represents the conventional placement of an ROI which is centered on the myocardium.

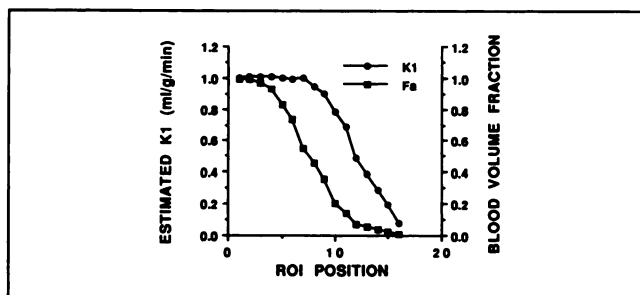


**FIGURE 5.** Noise-free simulation results. The curves represent the estimated  $K_1$  (circles) and  $F_a$  (squares) values as a function of ROI position. The original  $K_1$  value is 1.0 ml/g/min. Unbiased  $K_1$  values are observed for regions 1–8. Significant biases in  $K_1$  are observed for all other regions.

tion with either dipyridamole or adenosine. Microsphere blood flow was determined using the standard reference technique developed by Heymann et al. (21). Further details of the experimental protocols for this study are described by Muzik et al. (20).

## RESULTS

The performance of the ROI strategy described in this paper in the absence of statistical noise is shown in Figure 5. The parameter estimates for  $K_1$  and  $F_a$  are plotted as a function of the ROI position. In this plot, ROI position 0 represents left ventricle blood pool ( $F_a = 1.0$ ) and ROI position 20 is a point outside the epicardial surface of the heart ( $F_a = 0.0$ ). Unbiased estimates of  $K_1$  are achieved for ROIs which are located in the territory of the endocardium (regions 1–8). The blood volume estimates in this territory range from approximately 0.5–1.0. As the regions are moved across the midline of the myocardial wall and extend toward the epicardial surface of the heart, significant biases in the  $K_1$  estimate become obvious. Figure 6 shows the mean and standard deviation in the parameter estimates for studies which contain the equivalent of 1 million counts as a function of the ROI position. Results for regions 1–4 are not presented because the problem became ill-conditioned with blood volume fractions ap-

proaching 1.0. These results clearly demonstrate that the elimination of the resolution induced biases in  $K_1$  estimates is achieved at the expense of increasing the variance of the  $K_1$  estimate. In regions that have a large blood volume fraction (e.g., region 5), a positive bias in the  $K_1$  and  $k_2$  parameter estimates begins to appear. Histogram plots of the  $K_1$  estimates (Fig. 7) demonstrate that this bias is a result of a skewed distribution of the  $K_1$  estimates toward high  $K_1$  values. These results indicate that when the blood volume fraction is high, an increased noise sensitivity of  $K_1$  to overestimates of  $F_a$  is observed relative to the sensitivity of  $K_1$  to underestimates of  $F_a$ .

Figure 8 shows the relationship, which is observed between the bias and the variance in the kinetic model parameter estimates. Each data point in this plot represents an ROI location. The data points with very small standard deviations are near the epicardium and the points with large standard deviations are near the endocardium.

The fraction of the ROI volume occupied by blood ( $F_a$ ) is plotted as a function of myocardial wall thickness in Figure 9. Each of these data points represent a position at which 95% of the ROI volume contained either myocardial tissue or blood-pool (i.e., background contribution to the signal is 5%). The curves in Figure 9 represents results for image resolutions ranging from 4 mm to 14 mm FWHM. The coefficients of variation (COV) for the model parameter estimates for each model configuration tested are listed in Table 2. Comparison of the results in Table 2 with the data in Figure 9 enables the COV for kinetic model parameters to be estimated as a function of wall thickness and image resolution.

An example of the influence of the ROI position upon estimates of  $K_1$  is shown in Figure 10. The solid circles in each curve represent the measured ROI concentration and the solid lines are the fit to the data. The microsphere blood flow value calculated in this study was 1.24 ml/g/min. When an ROI is placed at a position which meets the assumptions of the model described in the methods, an unbiased estimate of  $K_1$  is achieved (region A in Figure 10). For regions which are centered on the myocardium

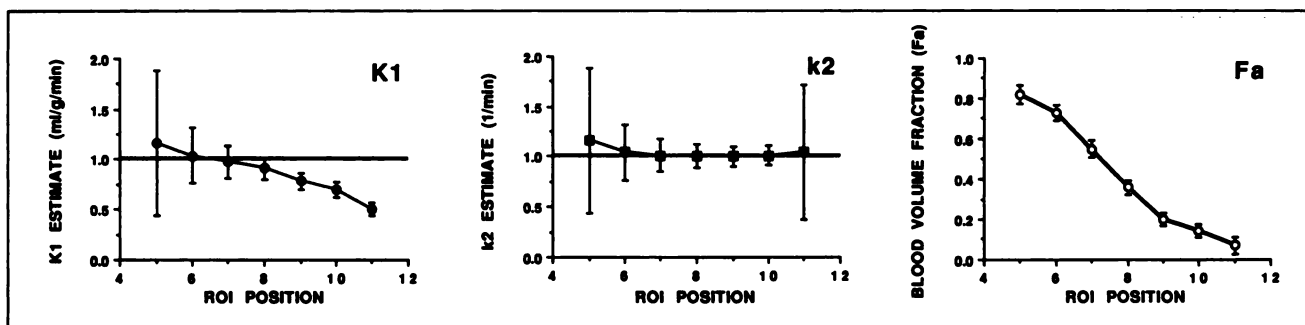


**FIGURE 6.** One million event simulation results. The curves show the mean and standard deviation of the kinetic model parameters as a function of ROI position. Each data point is based on 500 realizations of myocardial imaging studies containing 1 million events. These results are for model configuration A ( $K_1 = 1.0$  ml/g/min;  $k_2 = 1.0$  min<sup>-1</sup>). The solid lines in the  $K_1$  and  $k_2$  plots represent the true rate constant values in the simulation.

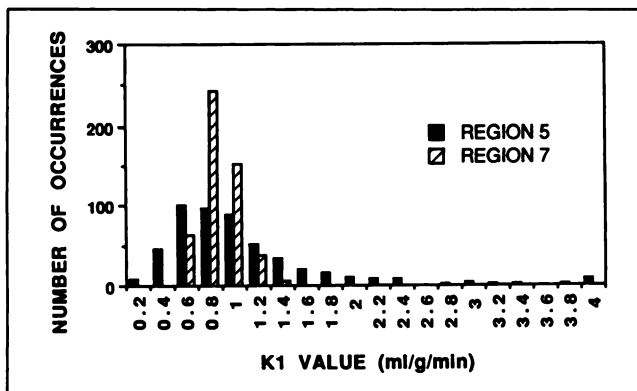


**FIGURE 7.**  $K_1$  histograms. The distribution of the  $K_1$  estimates for region 5 and region 7 are shown in Figure 6. The asymmetric distribution for region 5 leads to a positive bias in the mean  $K_1$  estimate.

or placed toward the epicardial surface of the heart, significant bias in the  $K_1$  estimates are observed (regions B and C in Figure 10).

The use of the ROI geometric model in the estimation of myocardial blood flow in dogs is presented in Figure 11. The plots show the correlation between the estimated blood flow and microsphere blood flow estimates. The solid squares represent the kinetic estimates using the ROI geometric model and the open squares represent the simulation results for model configurations E-J in Table 1. The slope of the relationship between the geometric model method and microspheres is 1.022 ( $r = 0.96$ ). The estimated errors in the simulation results are represented by the error bars. These simulation results are presented in Table 3.

## DISCUSSION

The results of the present work support the hypothesis that the resolution distortions (partial volume effect, spill-over) are the result of a single process and that correction procedures do not need to be separated into multiple steps. When the ROI volume contains only myocardial tissue

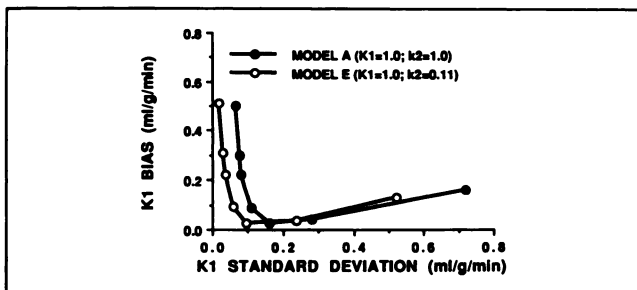


**FIGURE 8.** Bias versus standard deviation in  $K_1$ . The bias in  $K_1$  estimates is plotted against the  $K_1$  standard deviation as a function of ROI position for model configurations (A) (solid circles) and (E) (open circles). The data points with low standard deviations represent the epicardial surface of the heart, while the high standard deviations are in the endocardial territory of the heart.

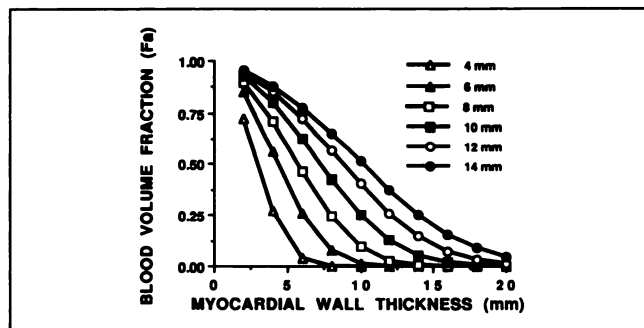


**FIGURE 9.** Myocardial wall thickness simulation results. The fraction of the ROI volume which is occupied by blood ( $F_b$ ) is plotted against the wall thickness of the myocardium for ROIs that are positioned so that 95% of the ROI volume contains either myocardium or blood. Results are presented for PET image resolutions ranging from 4 to 14 mm FWHM.

and blood, the distortion of measured time-activity curves can be represented by a single term in the geometrical model of a ROI (Eq. 7). Determination of this term, the fraction of the ROI volume occupied by blood ( $F_b$ ), by either measurements or parameter estimation procedures eliminates the resolution distortions in the kinetic data. In Figure 5, the performance of this approach on noise-free simulated PET data is presented. As the ROIs are placed on the image data in positions which meet the assumptions used to derive Equation 7, the bias in the scale parameter ( $K_1$ ) of the model disappears. When pseudorandom noise is added to the simulated PET data, it becomes evident that the reduction of resolution induced biases in model parameters is at the expense of increasing variance (Fig. 6). The plots in Figure 6 also demonstrate that positive biases in the scale-related kinetic model parameters begin to occur when the blood fraction of the ROI volume becomes large. The distribution of the scale-related parameter ( $K_1$ ) for ROIs with large  $F_b$ s compared to ROIs with well behaved parameter estimates is shown in Figure 7. This plot demonstrates that as the blood volume fraction becomes large, the noise sensitivity of the method is much greater for overestimates of  $F_b$  than underestimates of  $F_b$ . Therefore, the distribution of  $K_1$  estimates becomes skewed toward the high values leading to a bias in the mean value for multiple trials. The strong positive correlation between  $F_b$  and the scale parameter of the model, which is imposed by the form of Equation 7, is responsible for the large variation in the kinetic model parameter estimates when  $F_b$  becomes large. Thus, an obvious consequence is the tradeoff that must be made between bias and variance in the scale-related model parameters. In Figure 8, the bias in  $K_1$  is plotted against the standard deviation of  $K_1$ . Clearly an optimal ROI position can be selected that minimizes the combined effects of bias and variance. However, the selection of an ROI strategy should be based upon the objectives of the PET study. In studies that compare physiology under altered states in a single individual, it would be preferable to accept bias in param-

**TABLE 2**  
Kinetic Model Parameter Coefficients of Variation

| Figure 10: Model Parameters, Coefficients of Variation |             |       |       |             |       |       |             |       |       |             |       |       |             |       |       |
|--|-------------|-------|-------|-------------|-------|-------|-------------|-------|-------|-------------|-------|-------|-------------|-------|-------|
| $F_a$  | Model A COV |       |       | Model B COV |       |       | Model C COV |       |       | Model D COV |       |       | Model E COV |       |       |
|  | $K_1$       | $k_2$ | $F_a$ | $K_1$       | $k_2$ | $F_a$ | $K_1$       | $k_2$ | $F_a$ | $K_1$       | $k_2$ | $F_a$ | $K_1$       | $k_2$ | $F_a$ |
| 0.82   | 61.8        | 62.1  | 5.3   | 32.4        | 32.4  | 5.9   | 31.9        | 10.5  | 6.1   | 45.1        | 10.4  | 6.9   | 46.0        | 12.8  | 7.0   |
| 0.73   | 26.8        | 26.5  | 5.5   | 13.4        | 9.3   | 6.0   | 17.2        | 7.3   | 6.7   | 18.1        | 6.4   | 7.1   | 23.1        | 6.6   | 7.7   |
| 0.55   | 16.4        | 16.1  | 7.5   | 7.0         | 6.0   | 8.1   | 8.7         | 4.2   | 8.9   | 10.3        | 4.0   | 10.3  | 9.7         | 4.3   | 9.5   |
| 0.36   | 11.9        | 11.4  | 9.8   | 5.1         | 4.2   | 11.2  | 5.3         | 3.3   | 12.1  | 6.2         | 2.9   | 13.0  | 6.5         | 3.1   | 13.3  |
| 0.20   | 10.7        | 9.9   | 16.7  | 4.3         | 3.9   | 18.2  | 3.8         | 2.8   | 18.9  | 4.3         | 2.7   | 20.5  | 4.6         | 3.0   | 22.7  |
| 0.14   | 10.7        | 9.8   | 22.7  | 4.0         | 3.8   | 23.3  | 3.8         | 2.9   | 27.4  | 4.1         | 2.6   | 30.6  | 4.4         | 3.0   | 33.6  |
| 0.07   | 13.3        | 63.6  | 57.7  | 3.6         | 4.6   | 42.0  | 3.8         | 3.5   | 48.1  | 3.6         | 3.6   | 52.0  | 4.1         | 3.5   | 56.4  |

eter estimates in order to enhance the sensitivity to changes by decreasing the variance. On the other hand, if absolute quantitative values are necessary, the increased variance may be tolerated in order to eliminate bias. Nonetheless, these alternatives can be balanced, yielding kinetic model parameters that are essentially free of resolution distortion bias and have acceptable levels of variance.

An important element of this method is the ability to uniquely isolate the blood and tissue curve shapes in the parameter estimation procedure. In Tables 2 and 3, the COV of the parameter estimates are listed as a function of the curve tissue shapes which were defined by the model configurations in Table 1. Each of these studies is based upon the noise equivalent of 1 million events. It is evident that an optimal relationship exists between the shape of the input function and the shape of the tissue curve for

the isolation of scale related model parameters ( $K_1$ ). When the tracer behavior is similar to an inert freely diffusible substance with rapid tissue washout characteristics (model A, Table 1), the blood and tissue curves have similar shapes and the kinetic isolation of the tissue and blood components of the measured data becomes difficult. This leads to an increased variability in the kinetic model parameter estimates. As the tissue curve shapes become more kinetically distinct from the blood curve shape, the kinetic isolation of each component is more reliably determined. This results in a decrease in the variance of kinetic model parameters. In the simulation studies presented in this paper, a constant equivalent of 1 million counts was used in each imaging sequence. Therefore, as  $k_2$  became small in the simulations, the scale of the blood curve was reduced so that it contributed fewer counts to the study. This leads

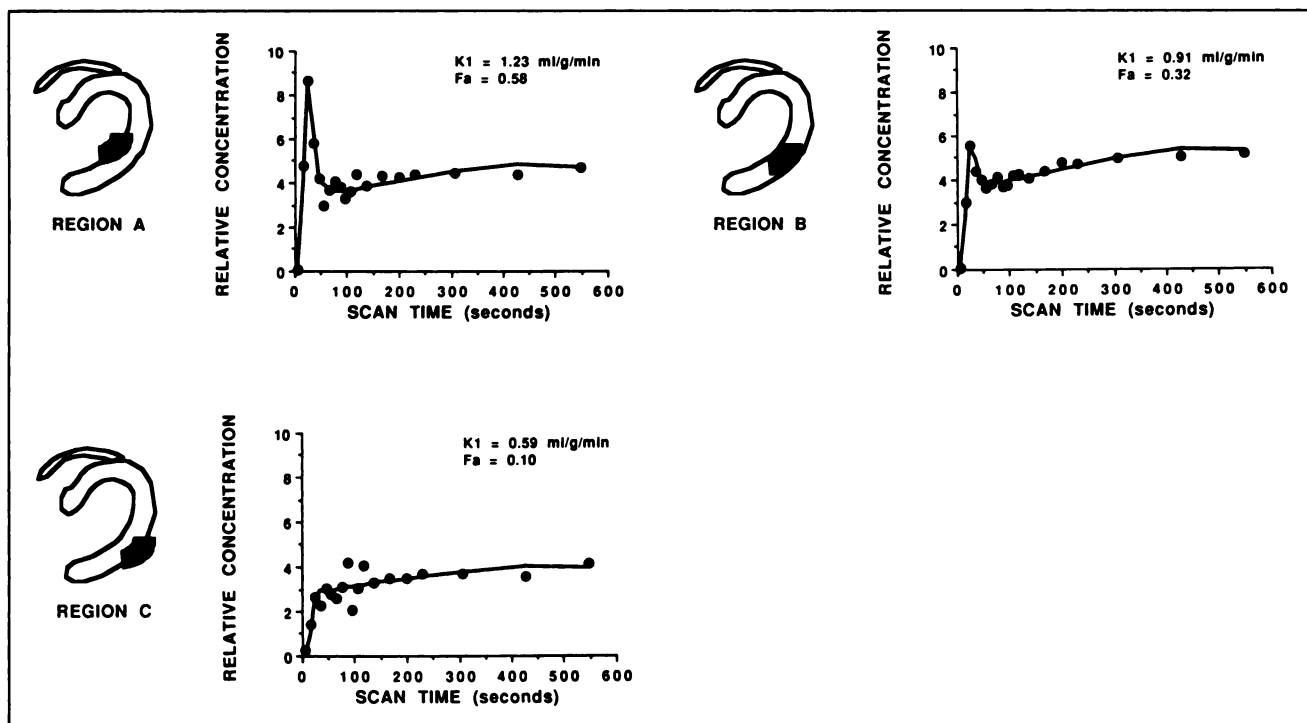


**FIGURE 10.** Nitrogen-13-ammonia regression plots. Regression plots for three ROI positions in a single dog study are shown. The figures on the left hand side demonstrate the relative ROI position on the myocardium. The estimated  $K_1$  and  $F_a$  values for each region are indicated in the top right hand corner of each plot. The microsphere determined blood flow in this study was 1.24 ml/g/min.

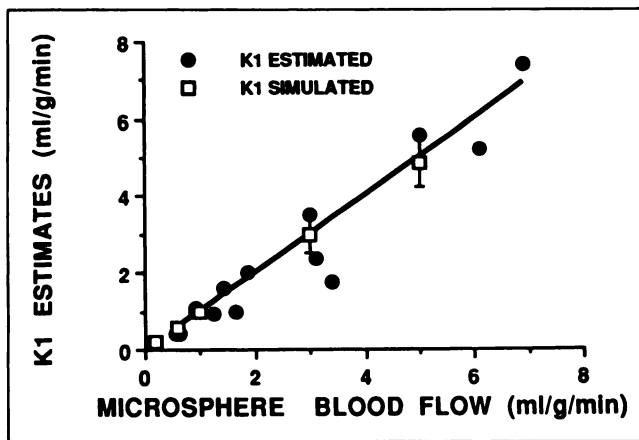


**FIGURE 11.** Nitrogen-13-ammonia  $K_1$  estimates versus microsphere blood flow. The estimated  $K_1$  values for a series of eight dogs (14 individual flow states) are plotted as a function of microsphere measured myocardial blood flow. The solid line is a line of identity (slope = 1.0). The solid circles are the results achieved using the ROI strategy. The open squares with error bars represent the simulation results for model configurations E-I (Table 1). A strong correlation between  $K_1$  and the microsphere blood flow was observed (slope = 1.022, intercept = -0.18,  $r = 0.96$ ).

to an increased variability in the  $F_a$  estimate and therefore an increased variability in  $K_1$  estimates. This effect is observed in Table 2. The properties of the ROI strategy described in these results indicate that careful selection among several potential tracers for a given application based upon the relative tissue and blood kinetics may significantly improve the estimation of kinetic model parameters.

A common consequence of myocardial disease is the loss of contractile function and subsequent thinning of the myocardial wall. This phenomenon typically will increase the distortions related to image resolution. The influence of wall thinning upon the ROI data analysis strategy described in this paper can be appreciated by examining the data in Figure 9. As the wall of the myocardium thins, the optimal ROI locations must be pushed further toward the endocardial surface of the heart in order to meet the assumptions of the ROI geometric model. Therefore, as the blood fraction of the ROI volume ( $F_a$ ) becomes large, the variance in the scale related model parameter ( $K_1$ ) also becomes large. Comparison of the data in Figure 9 with the data in Table 2 enables the assessment of myocardial

wall thickness limitations as a function of image resolution. For example, if approximately 20%–25% COV represent an acceptable upper limit, then the maximum blood volume fraction of an ROI volume must be in the 0.70–0.75 range (actual limit is sensitive to the blood and tissue tracer kinetics). In Figure 9, one can observe that this blood volume fraction is achieved when the thickness of the myocardium is approximately half the image resolution (FWHM). Analysis of regions where the wall thickness is less than half the image resolution will probably lead to highly variable results making the PET data very difficult to interpret. In conventional PET data acquisition protocols (non-gated) the motion of the heart limits the effective image resolution to approximately 10 mm FWHM. Therefore, it is anticipated that analysis of myocardial walls less than 5 mm thick may require the use of cardiac gating in order for optimal results to be achieved. Experimental verification of these observations is required.

The data in Figures 10 and 11 demonstrate the elimination of resolution induced bias in kinetic PET studies of the heart using the ROI strategy described in this work. The regression plots in Figure 10 demonstrate the ability of this model to describe measured ROI tissue curves for each of the ROI positions tested. The  $K_1$  estimate for region A is equivalent to the microsphere measured blood flow in this dog. In regions B and C, the assumptions of the model description are not met resulting in underestimation of the  $K_1$  or blood flow value. The data in Figure 11 clearly show the high degree of correlation which is achieved between the  $K_1$  estimates and microsphere determined blood flow over a wide blood flow range in dogs when optimized ROIs are utilized. Figure 11 also shows the results of the PET simulation studies which predict the observed experimental results.

The assumptions which must be met for the ROI strategy developed in this work to be successful dictate the definition of ROIs which are heavily weighted by the endocardium. This will result in a loss of sensitivity to signal changes which occur predominately in the epicardium. The ramification of this loss of sensitivity is study specific and must be evaluated for each class of study performed.

## CONCLUSION

The results of this study demonstrate the elimination of resolution induced biases in kinetic model parameters for the heart through the use of ROI data analysis strategies and simple models of the ROI volume representation in physical space. The removal of the resolution distortions (partial volume effect and spillover) is achieved at the expense of increasing the variance of individual parameter estimates. In the application of these methods, careful attention must be given to the objectives of the PET study and the tradeoff between parameter estimate bias and variance. Nonetheless, this study demonstrates that the bias and variance can be balanced, yielding estimates of

**TABLE 3**  
Simulation Study Parameter Estimates

| Model | $K_1$ (ml/g/min) | $k_2$ (min <sup>-1</sup> ) | $F_a$        |
|-------|------------------|----------------------------|--------------|
| F     | 0.19 ± 0.01      | 0.022 ± 0.004              | 0.55 ± 0.032 |
| G     | 0.58 ± 0.05      | 0.067 ± 0.004              | 0.55 ± 0.046 |
| E     | 0.97 ± 0.10      | 0.11 ± 0.005               | 0.55 ± 0.052 |
| H     | 2.97 ± 0.46      | 0.33 ± 0.015               | 0.55 ± 0.077 |
| I     | 4.87 ± 0.62      | 0.55 ± 0.030               | 0.55 ± 0.079 |

myocardial physiology that are essentially free of resolution-related distortions.

## ACKNOWLEDGMENTS

The authors would like to thank the Division of Nuclear Medicine, the PET Chemistry/Cyclotron staff, and the Cardiac PET group at the University of Michigan for providing the resources necessary to complete this work. We would also like to thank Dr. Markus Schwaiger for many helpful discussions regarding this work. The secretarial assistance of Patricia Haines in preparation of the manuscript is greatly appreciated. This work was supported in part by the National Institutes of Health, Bethesda, MD (R01 HL41047-01) and the Department of Energy, Washington, DC (DOE 89-035 and DOE DE GF02-87ER).

## REFERENCES

- Schelbert HR, Schwaiger M. PET Studies of the heart. In: Phelps M, Mazziotta J, Schelbert H, eds. *Positron emission tomography and autoradiography: principles and applications for the brain and heart*. New York: Raven Press; 1986;581-661.
- Hoffman EJ, Phelps ME, Wisenberg G, Schelbert HR, Kuhl DE. Electrocardiographic gating in positron emission computed tomography. *J Comp Assist Tomogr* 1979;3:733-739.
- Hoffman EJ, Huang SC, Phelps ME. Quantitation in positron emission tomography: 1. Effect of object size. *J Comput Assist Tomogr* 1979;3:299-308.
- Ter-Pogossian MM, Bergmann SR, Sobel BE. Influence of cardiac and respiratory motion on tomographic reconstructions of the heart: implication for quantitative nuclear cardiology. *J Comput Assist Tomogr* 1982;6:1148-1155.
- Wisenberg G, Schelbert HR, Hoffman EJ, et al. In vivo quantitation of regional myocardial blood flow by positron-emission computed tomography. *Circulation* 1981;63:1248-1258.
- Henze E, Huang SC, Ratib O, Hoffman E, Phelps ME, Schelbert HR. Measurement of regional tissue and blood radiotracer concentrations from serial tomographic images of the heart. *J Nucl Med* 1983;24:987-996.
- Wilson AR, Shea MJ, De Landsheere CM, et al. Validation of quantitation of regional myocardial blood flow in vivo with  $^{11}\text{C}$ -labeled human albumin microspheres and positron emission tomography. *Circulation* 1984;70:717-723.
- Bergmann SR, Fox KA, Rand AL, et al. Quantification of regional myocardial blood flow in vivo with  $\text{H}_2^{15}\text{O}$ . *Circulation* 1984;70:724-733.
- Huang SC, Schwaiger M, Carson RE, et al. Quantitative measurement of myocardial blood flow with oxygen-15-water and positron computed tomography: an assessment of potential and problems. *J Nucl Med* 1985;26:616-625.
- Knabb RM, Fox KA, Sobel RE, Bergmann SR. Characterization of the functional significance of subcritical coronary stenoses with  $\text{H}_2^{15}\text{O}$  and positron emission tomography. *Circulation* 1985;7:1271-1287.
- Iida H, Kanno I, Takahashi A, et al. Measurement of absolute myocardial blood flow with  $\text{H}_2^{15}\text{O}$  and dynamic positron emission tomography. Strategy for quantification in relation to the partial-volume effect. *Circulation* 1988;78:104-115.
- Bergmann SR, Herrero P, Markham J, Weinheimer CJ, Walsh MN. Noninvasive quantitation of myocardial blood flow in human subjects with oxygen-15-labeled water and positron emission tomography. *J Am Coll Cardiol* 1989;14(3):639-652.
- Krivokapich J, Smith GT, Huang S-C, Hoffman EJ, Ratib O, Phelps ME, Schelbert HR.  $^{13}\text{N}$  ammonia myocardial imaging at rest and with exercise in normal volunteers: quantification of absolute myocardial perfusion with dynamic positron emission tomography. *Circulation* 1989;80:1328-1337.
- Hutchins GD, Schwaiger M, Rosenspire KC, Krivokapich J, Schelbert H, Kuhl DE. Noninvasive quantification of regional blood flow in the human heart using N-13 ammonia and dynamic positron emission tomographic imaging. *J Am Coll Cardiol* 1990;15(5):1032-1042.
- Araujo LI, Lammertsma AA, Rhodes CG, et al. Noninvasive quantification of regional myocardial blood flow in coronary artery disease with oxygen-15-labeled carbon dioxide inhalation and positron emission tomography. *Circulation* 1991;83:875-885.
- Hutchins GD. Physiologic signal detection in positron emission tomography. In: DE Kuhl, ed. *Frontiers in nuclear medicine: in vivo imaging of neurotransmitter functions in brain, heart and tumors*. Washington, DC: American College of Nuclear Physicians; 1990;141-155.
- Huesman RH. A new fast algorithm for the evaluation of regions of interest and statistical uncertainty in computed tomography. *Phys Med Biol* 1984;29(5):543-552.
- Hutchins GD, Hichwa RD, Koeppel RA. A continuous flow input function detector for  $\text{H}_2^{15}\text{O}$  blood flow studies in positron emission tomography. *IEEE Trans Nucl Sci* 1986;NS-33:546-549.
- Marquardt DW. An algorithm for least-squares estimation of non-linear parameters. *J Soc Indust Appl Math* 1963;11:431-441.
- Muzik O, Beanlands R, Hutchins G, et al. Experimental validation of a tracer kinetic model for N-13 ammonia in comparison to O-15 water for quantification of myocardial blood flow [Abstract]. *J Nucl Med* 1991;32:926.
- Heymann MA, Payne BD, Hoffman JE, Rudolph AM. Blood flow measurements with radionuclide labeled particles. *Prog Cardiovasc Dis* 1977;20:55-79.